JOURNAL OF THE SOUTHEASTERN ASSOCIATION FOR RESEARCH IN ASTRONOMY, **2**, 39-46, 2008 MAY 1

COMPARING IMAGES OF SEYFERT GALAXIES IN MULTIPLE BANDS

RYAN TERRIEN [1]
Carleton College, 1 North College St., Northfield, MN 55057

ERIC PERLMAN
Florida Institute of Technology, 150 W. University Blvd., Melbourne, FL 32901

CHRISTOPHER PACKHAM AND CHARLES TELESCO
Astronomy Department, University of Florida, Gainesville, FL 32611

JAMES RADOMSKI
Gemini Observatory, Southern Operations Center, La Serena, Chile

AND

RACHEL MASON
Gemini Observatory, Northern Operations Center, Hilo, HI 96720

ABSTRACT

Galaxies with Active Galactic Nuclei (AGN) are expected to host a considerable amount of gas and dust that emit strongly in the mid-infrared (MIR) and can be related to structures seen in other bands. This dust can either be associated with the AGN phenomenon itself or concentrated in star formation regions on a variety of scales. We quantify and examine the spatial cross-correlation of the extended structure ($>$ 100pc from nucleus) in various emission line images, X-ray images, and MIR images of a sample of five Seyfert galaxies. Previous studies have determined that each object in the sample shows thermal emission from warm dust that is primarily heated by either the AGN central engine or by star formation. We cannot define any trends with such a small sample, but we find that both varieties have significant correlation between their Paα and MIR images, and the AGN-dominated galaxies usually have significnt correlation between their OIII images and MIR images. We find only one case of significant correlation between the X-ray and MIR images, in an object dominated by star formation.
Subject headings: infrared: galaxies — methods: statistical — galaxies: Seyfert

1. INTRODUCTION

According to the unified scheme, AGNs host a dusty torus that surrounds the powerful central engine and limits the area outside the nucleus that is directly in view of the central engine to a biconical region known as the narrow line region (NLR) Antonucci (1993). Hot gas in the NLR, such as OIII, is ionized by the central engine and is often observed in distinctly conical shapes. Dust in this area can also be heated by the continuum emission from the central engine, causing it to emit a thermal continuum in the mid-infrared (MIR) (Almudena Prieto et al. 2001). Alternatively, since galaxy mergers are known to cause bursts of star formation and may also trigger AGN, we may expect that the warm dust is being heated by star formation (Verma et al. 2005). Many active galaxies show extended star-forming regions with comparable luminosities to the nuclei themselves.

Clearly visible in the overall spectral energy distribution (SED) of many AGNs, this thermal emission from warm dust produces a notable feature known as the infrared (IR) bump just longward of 1 μm and lasting more than two decades in frequency. This thermal bump shares the mid-infrared band (MIR) with a number of other emission features, such as polycyclic aromatic hydrocarbon (PAH) lines, several fine structure lines, and silicate features (Verma et al. 2005). IR emission can also come from the dusty torus, but this possibility is not discussed in this study because it would be on a relatively small scale.

In addition to its many emission characteristics, a low susceptibility to scattering makes the MIR a promising band in which to observe AGNs. However, observing AGNs in the MIR is relatively young compared to the observing in the near infrared (NIR), optical, radio, and X-ray bands. These other bands have revealed jets, ionization cones, and other structural aspects that hint at a significant amount of dust being present around the AGN (Antonucci 1993), so observing AGNs in the MIR could provide important details about their structure.

Imaging AGNs in the MIR can provide direct information about extended dust structures and may even provide a direct SFR indicator due to the heating of PAHs by star formation regions (Alonso-Herrero et al. 2006). To further understand how MIR observations of AGNs might be analyzed, it is important to quantify and explain the spatial relationship between structures seen in the MIR and structures seen in other bands.

To this end, we obtained archival images of five Seyfert galaxies from a variety of observations and computed the spatial cross-correlation of various near-infrared (NIR) and optical emission line images (e.g. Paα, OIII, H_2) compared to MIR images, and of X-ray images compared to MIR im-

[1] Southeastern Association for Research in Astronomy (SARA) NSF-REU Summer Intern
Electronic address: terrienr@carleton.edu; eperlman@fit.edu

ages. Our data consisted of images from multiple unrelated observations performed by instruments on HST, Chandra, and Gemini. The objects used in the final analysis are IC5063 (Sy2), NGC 1097 (Sy1), NGC 4151 (Sy1.5), NGC 4388 (Sy2), and NGC 7130 (Sy2). These objects were chosen because they had been thoroughly studied and because they exemplified a range of phenomena associated with AGNs. For each object, previous studies have suggested the likely dominant source of MIR emission: either dust being heated directly by the AGN central engine (Young et al. 2007; Radomski et al. 2003; Schmitt et al. 2003) of the unified scheme or dust being heated by star formation (Mason et al. 2007; Alonso-Herrero et al. 2006).

2. OBSERVATIONS, REDUCTION, AND ANALYSIS

Our data was from a variety of sources and had to be reduced and made to conform to the same resolution and PSF size, so this section will detail the observations, then the instruments and reduction techniques for each band, and finally the analytical methods.

2.1. *Observations*

Observational details are shown in Table 1. The datasets from NGC 2992 and NGC 7582 are included although they were not useful in the final analysis.

2.2. *Mid-IR*

We obtained MIR observations from Michelle, OSCIR, and the Thermal-Region Camera Spectrograph (T-ReCS), MIR imagers/spectrometers on the Gemini North and South telescopes. Since MIR images are paramount in this study, it is important to note that the Gemini telescopes necessarily have a different observing technique from other ground-based telescopes because of the noise associated with observing in the IR. This stems from the fact that the entire surrounding environment is significantly brighter at IR wavelengths than the object being observed. During each observation, the Gemini telescopes automatically subtract background exposures at a frequency of a few Hz and automatically subtract telescope noise a few times per minute. The exposures necessary for this process are obtained by oscillating the secondary mirror to a position off the source (chopping) and by pointing the telescope at a position off the source (nodding). Gemini output data for each observation is a collection of several nods.

The MIR data, being the crux of this study and providing the limiting resolution and PSF size, were the most direct to reduce. The IRAF Gemini package provided the necessary routines. We first combined all the nods from an individual observation into a test image, excluding nods which were obviously compromised by noise or otherwise. We then reexamined each nod and excluded those nods in which the ellipticity of the source was more than twice the ellipticity of the source in the test image. If this process left only 4 nods or less, the ellipticity requirement was loosened to 3 times the ellipticity of the test image.

2.3. *Near-IR*

We obtained NIR data from the Near-Infrared Cameras NIC2 and NIC3 on the Near Infrared Camera and Multi-Object Spectrometer (NICMOS), an imager/spectrometer on HST.

NICMOS data were reduced with generic IRAF routines. NICMOS images have a smaller point spread function (PSF) than MIR images from Gemini instruments, so it was necessary to apply a Gaussian smoothing function to the NICMOS images in order to make their comparison meaningful. A sigma of about .94 pix was used to match the Gemini images.

2.4. *Optical*

We obtained optical data from the Wide Field Planetary Camera 2 (WFPC2) on HST.

WFPC2 data were reduced with the IRAF WFPC2 package. Multiple exposures were necessary to identify and remove cosmic ray events. After making a mosaic of the images from the PC chip and the three WF chips and increasing the pixel size of the PC chip to match the WF chips, we applied a Gaussian smoothing function with a sigma of about 9.44 pix in order to match the PSF size of the MIR images.

2.5. *X-ray*

We obtained X-ray data from the Advanced CCD Imaging Spectrometer (ACIS) on the Chandra X-ray telescope.

Chandra data were reduced using a combination of generic IRAF routines and CIAO routines. The event files recorded by ACIS were rebinned to a resolution of $0\farcs1/pix$ and split into three bands: soft(.2-1.5 keV), medium(1.5-2.5 keV), and hard(2.5-8 keV).

2.6. *General*

All images were then magnified to a standard resolution ($0\farcs1/pix$) and aligned assuming that the point of peak brightness in each image corresponded to the same point. Without astrometric data, this was taken to be the most accurate method of aligning the images, although it may present difficulties in objects like IC 5063, where extinction causes different brightness peaks for different wavelengths (Young et al. 2007).

2.7. *Analysis*

A routine was then developed around the correl_images function in the IDL astronomy package. This routine derived a correlation coefficient between a comparison image and an MIR image for x and y offsets of -40 to +40 pix. By deriving the correlation for situations when the images were obviously unaligned, we are able to visually define a level of insignificant correlation. This is useful because we have no formal way of deciding the statistical significance of our results.

Then, all the pixels within 100pc of the brightest point were replaced with 0, and the correlation coefficients were derived again. This allowed us to focus on the extended structure and ignore any correlation related to the nucleus, which is at least partly unresolved and spatially uninformative. All analysis in this study is concerned only with these images of the extended structure.

The correlation coefficients were displayed by plotting them as a histogram, and also as a surface, with the x and y coordinates corresponding to the displacement of the images and the z coordinate being the correlation coefficient. These displays allowed examination of the sharpness of the correlation peak and its height compared to the level of insignificance.

Finally, an image was constructed with a greyscale background being the MIR image of interest. Contours of the comparison image were overlaid in green. A red circle denoting the 100pc mark from the center was also overlaid. This image simply allowed the inspection of which structures were producing the correlation for a given pair of images.

TABLE 1
OBSERVATION INFORMATION

Target	Telescope	Instrument	Plate Scale("/pix)[a]	Date	Exp. Time(s)	Filter	Obs. ID[b]
IC 5063	HST	NIC3	0.203	04/18/97	255.95	F190N	N3UY01080
IC 5063	HST	NIC3	0.203	04/19/97	255.95	F215N	N3UY01090
IC 5063	Gemini-South	T-ReCS	0.09	05/21/05	304.1	Qa-18.3um	S20050521S0071
IC 5063	Gemini-South	T-ReCS	0.09	05/21/05	130.3	Si2-8.8um	S20050521S0070
IC 5063	Gemini-South	T-ReCS	0.09	07/18/05	130.3	Si2-8.8um	S20050718S0122
IC 5063	Gemini-South	T-ReCS	0.09	07/18/05	304.1	Qa-18.3um	RS20050718S0123
IC 5063	HST	WFPC2	0.0455	04/06/01	300	FR533N	U67L5201M
NGC 1097	Chandra	ACIS-S	0.492	01/28/01	5410	···	1611
NGC 1097	Chandra	ACIS-S	0.492	01/28/01	6330	···	2339
NGC 1097	HST	NIC3	0.203	06/05/07	159.96	F187N	N9WU07010
NGC 1097	HST	NIC3	0.203	06/05/07	223.96	F190N	N9WU07020
NGC 1097	Gemini-South	T-ReCS	0.09	08/21/05	456.1	Si5-11.7um	S20050821S0091
NGC 1097	Gemini-South	T-ReCS	0.09	09/17/05	456.1	Si5-11.7um	S20050917S0132
NGC 1097	Gemini-South	T-ReCS	0.09	09/16/05	912.2	Qa-18.3um	S20050916S0157
NGC 4151	Chandra	ACIS-S	0.492	12/04/99	2.05	···	347
NGC 4151	Chandra	ACIS-S	0.492	03/07/00	27.95	···	348
NGC 4151	Chandra	ACIS-S	0.492	03/06/00	11.3	···	372
NGC 4151	HST	NIC2	0.076	05/22/98	127.96	F187N	N4HK13010
NGC 4151	HST	NIC2	0.076	05/22/98	127.96	F190N	N4HK13040
NGC 4151	HST	NIC3	0.203	01/15/98	127.96	F196N	N4HK17010
NGC 4151	HST	NIC3	0.203	01/15/98	127.96	F200N	N4HK17040
NGC 4151	HST	WFPC2	0.0455	01/22/95	260	F502N	U2I50101T
NGC 4151	HST	WFPC2	0.0455	01/22/95	600	F502N	U2I50102T
NGC 4151	HST	WFPC2	0.0455	01/22/95	10	F502N	U2I50103T
NGC 4151	HST	WFPC2	0.0455	07/15/97	900	F502N	U423A103M
NGC 4151	HST	WFPC2	0.0455	07/15/97	900	F502N	U423A104M
NGC 4151	HST	WFPC2	0.0455	04/05/98	350	F656N	U4230608R
NGC 4151	HST	WFPC2	0.0455	04/05/98	350	F656N	U4230609R
NGC 4151	Gemini-North	OSCIR	0.084	05/07/01	360	N-10.8 um	···
NGC 4388	Chandra	ACIS-S	0.492	06/08/01	20230	···	1619
NGC 4388	Gemini-North	Michelle	0.101	05/14/06	945	No filter	N20060514S0105
NGC 4388	Gemini-North	Michelle	0.101	05/14/06	2853	No filter	N20060514S0108
NGC 4388	Gemini-North	Michelle	0.101	05/12/06	733	F185B9B	N20060512S0144
NGC 4388	Gemini-North	Michelle	0.101	05/12/06	2841	No filter	N20060512S0157
NGC 4388	HST	WFPC2	0.0455	03/27/96	140	FR680N	U2XI0207T
NGC 4388	HST	WFPC2	0.0455	03/27/96	140	FR680N	U2XI0208T
NGC 4388	HST	WFPC2	0.0455	03/27/96	140	FR533N	U2XI0201T
NGC 4388	HST	WFPC2	0.0455	03/27/96	140	FR533N	U2XI0202T
NGC 4388	HST	WFPC2	0.0455	03/27/96	140	FR533N	U2XI0203T
NGC 4388	HST	WFPC2	0.0455	03/27/96	140	FR533N	U2XI0204T
NGC 7130	Chandra	ACIS-S	0.492	10/23/01	39520	···	2188
NGC 7130	HST	NIC2	0.076	11/07/04	319.96	F190N	N8ZL25030
NGC 7130	HST	NIC2	0.076	11/07/04	287.96	F187N	N8ZL25040
NGC 7130	Gemini-South	T-ReCS	0.09	09/18/05	304.1	N-10.36um	S20050918S0033
NGC 7130	Gemini-South	T-ReCS	0.09	09/18/05	304.1	N-10.36um	S20050918S0034
NGC 7130	Gemini-South	T-ReCS	0.09	09/18/05	43.4	N-10.36um	S20050918S0035
NGC 2992	Chandra	ACIS-S	0.492	02/16/03	50180	···	3956
NGC 2992	Gemini-North	Michelle	0.101	03/25/07	2281	No filter	N20070325S0025
NGC 2992	Gemini-North	Michelle	0.101	03/23/07	2283	No filter	N20070323S0117
NGC 2992	Gemini-North	Michelle	0.101	05/12/06	2838	No filter	N20060512S0134
NGC 2992	Gemini-North	Michelle	0.101	05/12/06	730	F112B21	N20060512S0127
NGC 2992	Gemini-North	Michelle	0.101	03/25/07	2281	No filter	N20070325S0019
NGC 2992	Gemini-North	Michelle	0.101	05/12/06	1095	F185B9B	N20060512S0128
NGC 2992	HST	NIC3	0.203	10/14/98	207.89	F196N	n4sb08w1q
NGC 2992	HST	NIC3	0.203	10/14/98	207.89	F200N	n4sb08w5q
NGC 2992	HST	NIC3	0.203	10/14/98	207.89	F196N	n4sb08w9q
NGC 2992	HST	NIC3	0.203	10/14/98	207.89	F200N	n4sb08wdq
NGC 7582	Chandra	ACIS-S	0.492	10/14/00	13620	···	436
NGC 7582	Chandra	ACIS-S	0.492	10/15/00	5950	···	2319

NOTE. —Table 1 shows the details of the source datasets for this study. For NGC 2992, NGC 4151, and NGC 4388, all the observations that may have been used are listed; it is possible that some of them were not.

[a]For WFPC2 images, the source was always at least partly on the WF chips, so the pixel size of the PC chip was increased to match the WF chip pixel size.

[b]Obs IDs correspond to the dataset for HST data, the original file name for Gemini data, and the observation ID for chandra data.

3. RESULTS

3.1. *IC 5063*

The 18.3 μm and 8.8 μm emission images for IC 5063 show a source with considerable emission that extends out to about 300 pc from the nucleus and is roughly similar in all directions. There is no apparant elongation.

The Paα, H_2, and [OIII] emission line images were compared to 18.3 μm and 8.8 μm emission line images. The Paα and H_2 images behave similarly, producing significant correlation for both MIR wavelengths. [OIII] emission, however, produces weak correlation for both MIR bands (see Table 2). In Figure 1 we show the correlation data for Paα emission compared to 18.3 μm emission. Inspection of the images for Paα and H_2 provides little insight, as these emission lines simply form circles around the nucleus. However, it is interesting to note in the [OIII] image that there is little MIR extension along the ionization cones, as shown in Figure 2.

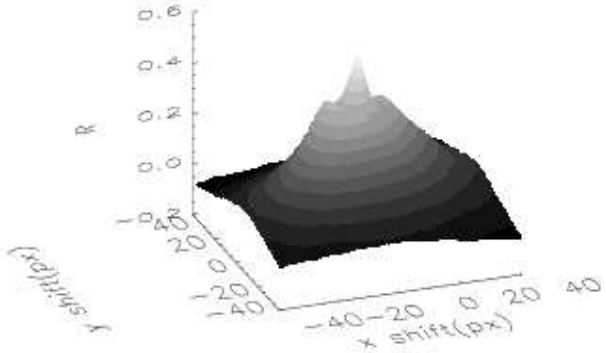

FIG. 1.—IC 5063: Correlation Coefficient Surface for Paα vs 18.3 μm. North is up, east is left.

Young et al. (2007) find that the most likely source of MIR emission in IC 5063 is dust in the NLR or an extended disc, heated by the AGN central engine. Our data suggest that hot gas and warm dust are spatially coincident in the extended region of interest, but that warm dust does not trace the OIII ionization cone as it might be expected to if it were associated with the NLR. Our data are consistent with the suggestion of Young et al. (2007) that the MIR-emitting dust is on the inner edge of an extended dusty disc.

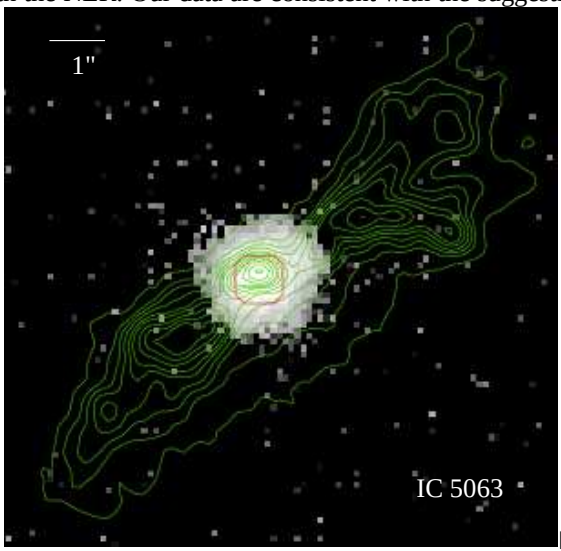

[h!]

FIG. 2.— IC 5063: Comparison image for OIII(contours) vs 18.3 μm(greyscale). Note the lack of MIR exension along the ionization cones that are clearly visible in OIII emission. North is up, east is left.

3.2. *NGC 1097*

The 11.6 μm and 18.3 μm emission images for NGC 1097 show a small, mostly unresolved nucleus that does not extend further than 100 pc from the nucleus in any direction. This nucleus is surrounded by a large starburst ring, more luminous in 11.6 μm than 18.3 μm, and just as luminous as the nucleus in knots to the north and west.

The Paα and X-ray images were compared to 11.6 μm and 18.3 μm emission. Significant correlation was only found between Paα and 11.6 μm emission, as shown in Table 2. Examination of the comparison images shows that nearly every knot in the starburst ring emits strongly in both Paα and 11.6 μm. In Figure 3 we show the correlation data for Paα emission vs 11.6 μm emission and in Figure 4 we show the comparison image for this pair.

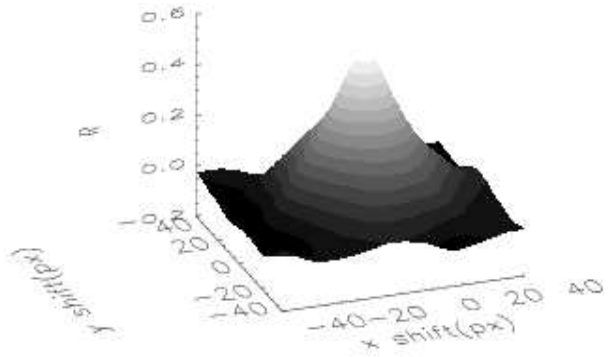

FIG. 3.—NGC 1097: Correlation Coefficient Surface for Paα vs 11.6 μm. North is up, east is left.

Given that Paα reliably traces star formation (Kennicutt 1998), our data suggest that much of the MIR emission at 11.6 μm is from dust being heated by star formation. Additionally, the 11.6 μm image likely contains the PAH band at approximately this wavelength, which is caused by PAHs being transiently heated by UV photons from star formation regions (Verma et al. 2005).

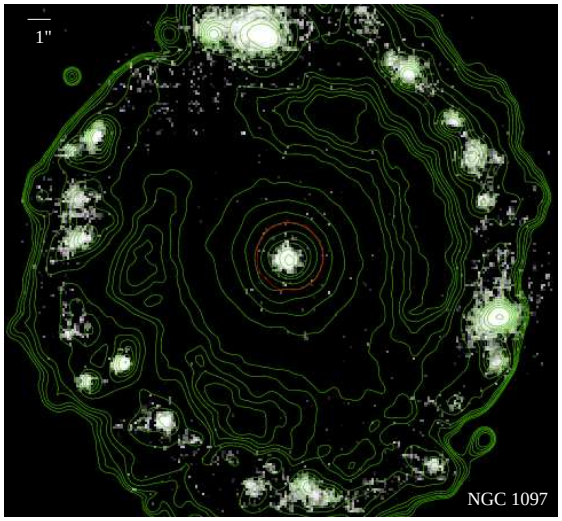

FIG. 4.— NGC 1097: Comparison image for Paα(contours) vs 11.6 μm(greyscale). Every MIR knot in the starburst ring is also visible in Paα emission. North is up, east is left.

TABLE 2
SELECTED CORRELATION COEFFICIENTS

Object	MIR Band(μm)	Paα	OIII	H_2	Hα	Soft X-rays
IC 5063	18.3	.585	.391	.722	···	···
IC 5063	8.80	.634	.401	.783	···	···
NGC 1097	11.6	.628	···	···	···	.033
NGC 1097	18.3	.235	···	···	···	.020
NGC 4151	N-band(λ7.70-12.97)	.324	.348	···	.347	.236
NGC 4388	N-band	···	.167	···	.116	.054
NGC 7130	N-band	.574	···	···	···	.446

NOTE. —Table 2 shows the pertinent correlation coeffi cients from each object. The numbers are the peak correlation coeffi cient for the images in corresponding row and column. For reference, the coeffi cients usually become completely insignifi cant if they are lower than .2.

3.3. *NGC 4151*

The N-band (λ7.70 μm-12.97 μm) MIR image shows a nucleus that does not extend much further than 100 pc from the nucleus in any direction. However, the source is clearly elongated in the northeast and southwest directions.

The Paα, [SiVI], [OIII], and Hα emission line images, as well as the X-ray bands, were all compared to an N-band (λ7.70 μm-12.97 μm) MIR image. Similar weak levels of correlation were found between all the emission line images and the MIR image, and no significant correlation was found relating to the X-ray images (see Table 2). Comparisons from Paα and [OIII] are representative. The extension of the nucleus in the MIR is in the same directions as the ionization cones visible in the [HII], [SiVI], [OIII], and Hα images. Figures 5 and 6 show the correlation data and comparison image for Paα emission vs N-band emission, and Figures 7 and 8 show the same for [OIII] emission vs N-band emission.

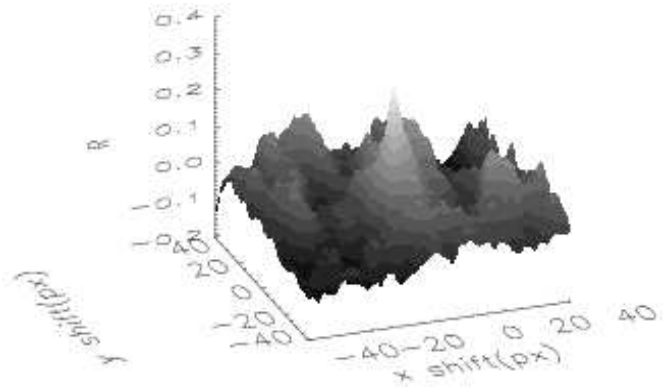

FIG. 5.—NGC 4151: Correlation Coefficient Surface for Paα vs N-band. North is up, east is left.

Radomski et al. (2003) find that the most likely source of MIR emission in NGC 4151 is dust in the NLR being heated by the AGN central engine. Our data agrees, as MIR emission appears mostly coincident wih emission from ionized gas ([HII], [SiVI], [OIII], Hα). It is important to note in this case that the analysis we performed was only concerned with the extension outside of 100 pc from the nucleus, because it is clear from the comparison image that a much stronger correlation coefficient could be derived from the inner, less resolved part of the nucleus.

3.4. *NGC 4388*

The N-band image shows a source that does not extend further than 100 pc from the nucleus in most directions, but has a very large extension to the southwest.

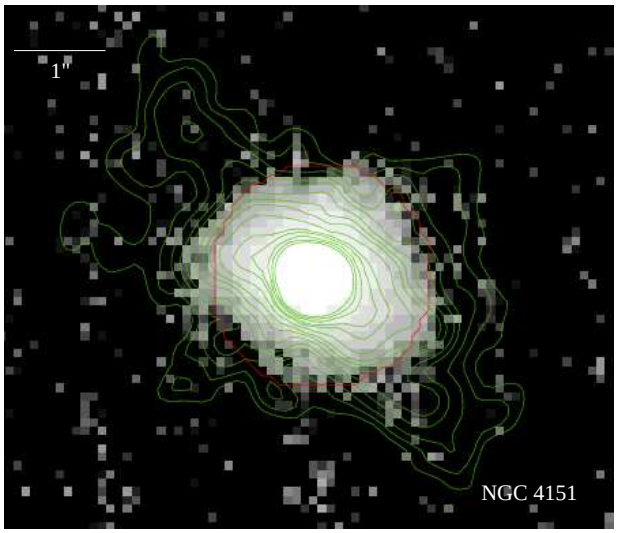

FIG. 6.— NGC 4151: Comparison image for Paα(contours) vs N-band(greyscale). There is clearly MIR extension along the ionization cone axis. North is up, east is left.

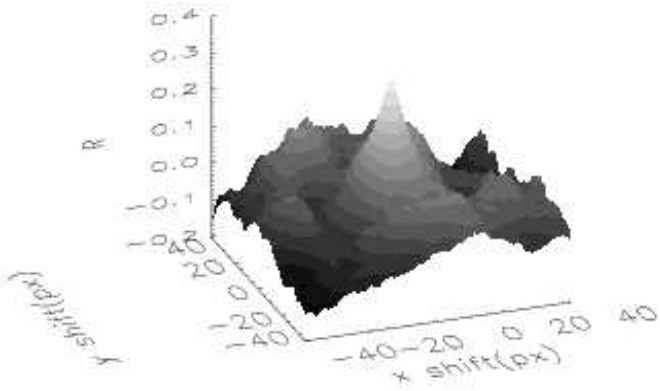

FIG. 7.—NGC 4151: Correlation Coefficient Surface for OIII vs N-band. North is up, east is left.

The Hα and [OIII] emission line images, as well as the X-ray images, were compared to an N-band MIR image. Significant correlation was not found for any of these comparisons, as shown in Table 2. This extension visible in the N-band image is coincident with one edge of the ionization cone visible in the emission line images. In Figures 9 and 10 we show the correlation data and comparison image for OIII emission vs N-band emission.

Schmitt et al. (2003) find that NGC 4388 has a large (1000pc) ionization cone opening southward. Our images suggest that most of the MIR emission is associated with

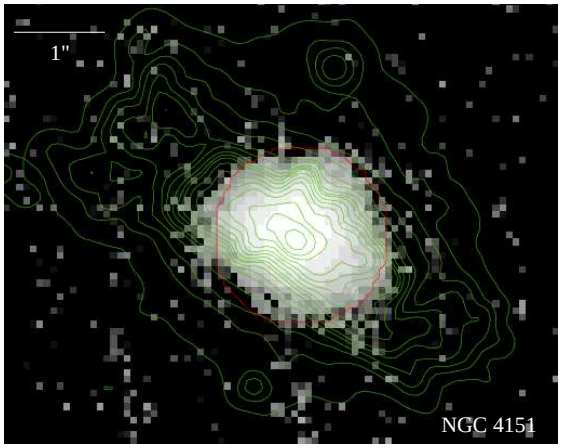

FIG. 8.— NGC 4151: Comparison image for OIII(contours) vs N-band(greyscale). Once again, there is clearly MIR extension along the ionization cone axis. North is up, east is left.

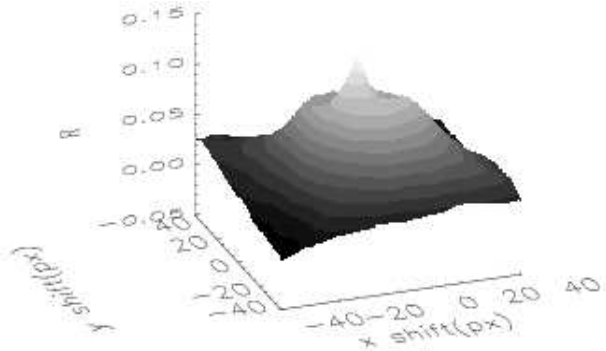

FIG. 9.—NGC 4388: Correlation Coefficient Surface for OIII vs N-band. North is up, east is left.

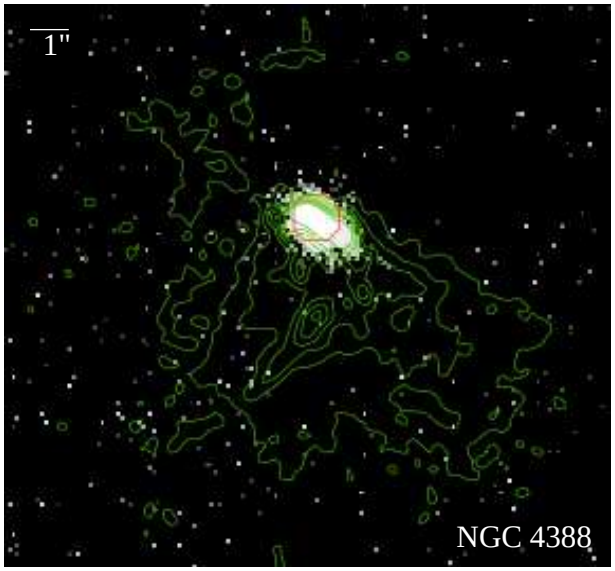

FIG. 10.— NGC 4388: Comparison image for OIII(contours) vs N-band(greyscale). MIR emission extends southwest, along one edge of the ionization cone. North is up, east is left.

this cone, and we therefore expect the MIR emission to be from warm dust in the NLR. This is presently unconfirmed, however, as there is no published MIR spectroscopic study of NGC 4388 and our numerical results show no significant correlation.

3.5. *NGC 7130*

The N-band image shows a central source with a slightly triangular shape that extends out to at least 300 pc from the nucleus. There is also a prominent knot of emission to the north, separated from the nucleus by several kiloparsecs.

The Paα emission line image and X-ray images were compared to an N-band MIR image. This object showed good correlation between the Paα emission and N-band emission images, and it was the only object to show any significant correlation between the X-ray images and the MIR image (see Table 2). In Figures 11 and 12 we show the correlation data and comparison

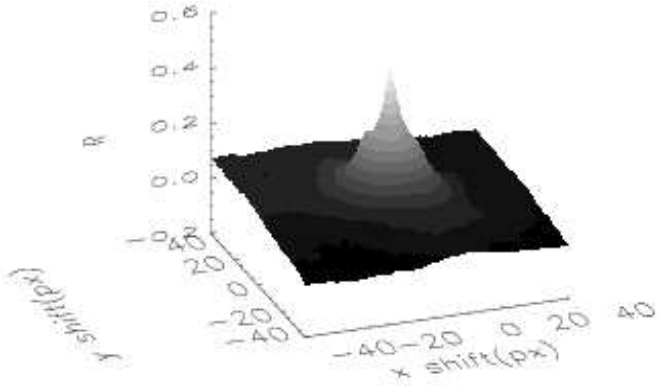

FIG. 11.—NGC 7130: Correlation Coefficient Surface for Paα vs N-band. North is up, east is left.

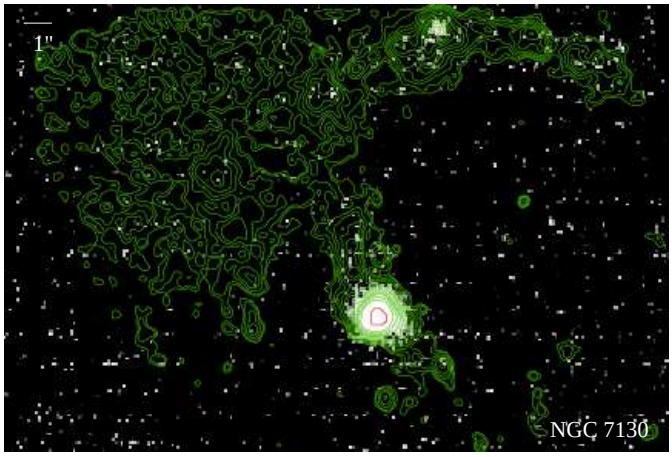

FIG. 12.— NGC 7130: Comparison image for Paα(contours) vs N-band(greyscale). Small parts of the arm extending northward are luminous in both the MIR and Paα bands. North is up, east is left.

image for Paα emission vs N-band emission, and in Figures 13 and 14 we show the same for soft X-ray emission vs N-band emission.

Alonso-Herrero et al. (2006) find that the MIR emission in NGC 7130 is probably dominated by dust heated by star formation. Our data support this finding, with several knots in the star-forming arm being coincident in the MIR and Paα images and a similar triangular extension of the nucleus. The soft X-ray images(.2-1.5 keV) also show a similar type of extension. This may be indicative of massive star formation near the nucleus. However, it is more likely that because this object is the furthest in the sample (65 mpc), the 100 pc limit

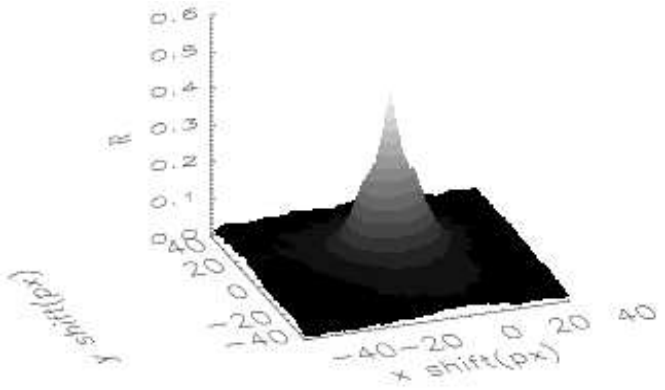

FIG. 13.—NGC 7130: Correlation Coefficient Surface for soft X-rays vs N-band. North is up, east is left.

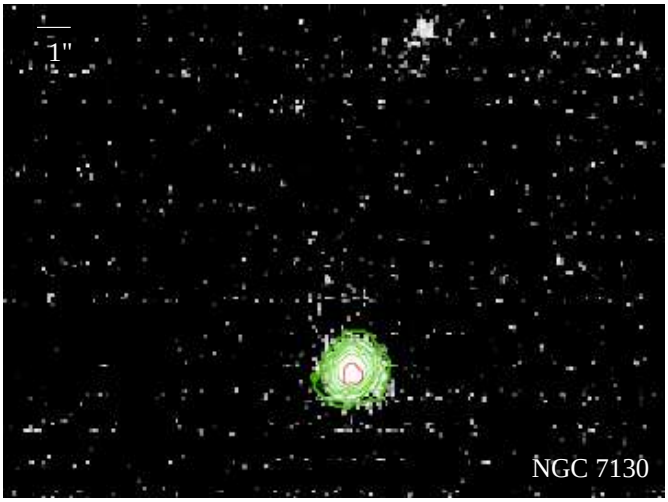

FIG. 14.—NGC 7130: Comparison image for soft X-rays(contours) vs N-band(greyscale). The nucleus has the same triangular extension in both the soft X-rays and N-band emission. North is up, east is left.

is itself not fully resolved and we therefore are finding correlation between the point sources in each band, which is not useful.

4. SUMMARY

We have quantified and examined the spatial cross-correlation between various emission line images, x-ray images, and MIR images of a sample of five Seyfert galaxies. In each case, the MIR emission was dominated by the warm dust thermal emission, with the dust being heated by either star formation or the AGN central engine. Certainly there were other MIR features present in some cases as well, such as the PAH emission seen in NGC 1097. We have concerned ourselves only with structures in these galaxies beyond 100pc from the nucleus.

We find that two out of three of our AGN engine-dominant objects (IC 5063, NGC 4151) show significant but weak correlation between [OIII] emission and MIR emission, while one (NGC 4388) shows none. We would expect strong correlation in this case because both the hot gas and the warm dust would need to be in the NLR, in view of the central engine. Possibly, the weak correlation is a result of the warm dust simply not extending as far as the hot gas, or perhaps the dust is heated preferentially only in certain areas of the NLR.

All the objects with Paα data available showed significant correlation between the Paα image and the MIR image. We expect a strong correlation between these two if the dust is being heated by star formation, and in the AGN engine-dominated objects this correlation may be indicative of some level of star formation remaining siginficant in heating the dust.

We find only one case (NGC 7130) out of four with X-ray data that shows any significant correlation between extended X-ray emission images and extended MIR emission images. This correlation, however, may be the result of the object being far enough away that even our 100 pc limit did not prevent the point sources from being correlated. With this taken into account, it seems that cross-correlating X-ray images with MIR images is not useful for examining extended structure.

Ultimately, we conclude that warm dust in AGN extended structure varies on an object by object basis. Most likely, there is always a combination of AGN engine-heated dust and star formation-heated dust producing the IR bump in AGN SEDs, but some objects will have one type clearly dominant over the other.

No correlation trends can be definitvely drawn from this small sample, although it seems to support the findings of previous spectroscopic and imaging studies of each particular object. In each of our objects, structures seen in the MIR can be directly associated with structures seen in other bands, which is promising for the future use of MIR imaging to probe AGNs. Larger samples and further analysis will be necessary in order to hone the use of spatial cross-correlation in this context.

This project was funded by a partnership between the National Science Foundation (NSF AST-0552798), Research Experiences for Undergraduates (REU), and the Department of Defense (DoD) ASSURE (Awards to Stimulate and Support Undergraduate Research Experiences) programs. This publication makes use of data from observations obtained at the Gemini Observatory (acquired through the Gemini Science Archive), which is operated by the Association of Universities for Research in Astronomy, Inc., under a cooperative agreement with the NSF on behalf of the Gemini partnership: the National Science Foundation (United States), the Particle Physics and Astronomy Research Council (United Kingdom), the National Research Council (Canada), CONICYT (Chile), the Australian Research Council (Australia), CNPq (Brazil) and CONICET (Argentina). This publication also makes use of data from observations made with the NASA/ESA Hubble Space Telescope, obtained from the data archive at the Space Telescope Science Institute. STScI is operated by the Association of Universities for Research in Astronomy, Inc. under NASA contract NAS 5-26555. We are grateful for the help of James Radomski and Los Piratas in obtaining and reducing the data.

REFERENCES

Alonso-Herrero, A., Colina, L., Packham, C., Díaz-Santos, T., Rieke, G. H., Radomski, J. T., & Telesco, C. M. 2006, ApJ, 652, L83
Almudena Prieto, M., Pérez-García, A., & Rodríguez-Espinosa, J. M. 2001, ArXiv Astrophysics e-prints, arXiv:astro-ph/0101103
Antonucci, R. 1993, ARA&A, 31, 473
Kennicutt, R. C., Jr. 1998, ARA&A, 36, 189
Mason, R. E., Levenson, N. A., Packham, C., Elitzur, M., Radomski, J., Petric, A. O., & Wright, G. S. 2007, ApJ, 659, 241
Radomski, J. T., Piña, R. K., Packham, C., Telesco, C. M., De Buizer, J. M., Fisher, R. S., & Robinson, A. 2003, ApJ, 587, 117
Schmitt, H. R., Donley, J. L., Antonucci, R. R. J., Hutchings, J. B., & Kinney, A. L. 2003, ApJS, 148, 327
Verma, A., Charmandaris, V., Klaas, U., Lutz, D., & Haas, M. 2005, Space Science Reviews, 119, 355
Young, S., Packham, C., Mason, R. E., Radomski, J. T., & Telesco, C. M. 2007, MNRAS, 378, 888